Coseismic or Landslide? The source of the 2018 Palu Tsunami

A.L. Williamson[1], D.M. Melgar[1], X Xu[2], and C.W.D. Milliner[3]

[1] University of Oregon, Department of Earth Sciences, Eugene, OR, USA.

[2] University of California San Diego, Scripps Institution of Oceanography, La Jolla, CA, USA.

[3] Jet Propulsion Laboratory, California Institute of Technology, Pasadena, CA, USA.

Corresponding Author: A.L. Williamson (awillia5 @ uoregon.edu)

Abstract

On 28 September, 2018, Indonesia was struck by a M_W 7.5 strike-slip earthquake. An unexpected tsunami followed, inundating nearby coastlines leading to extensive damage. Given the traditionally non-tsunamigenic mechanism, it is important to ascertain if the source of the tsunami is indeed from coseismic deformation, or something else, such as shaking induced landsliding. Here we determine the leading cause of the tsunami is a complex combination of both. We constrain the coseismic slip from the earthquake using static offsets from geodetic observations and validate the resultant "coseismic-only" tsunami to observations from tide gauge and survey data. This model alone, while fitting some localized run-up measurements overall fails to reproduce both the timing and scale of the tsunami. We also model coastal collapses identified through rapidly acquired satellite imagery and video footage as well as explore the possibility of submarine landsliding using tsunami ray tracing. The tsunami model results from the landslide sources, in conjunction with the coseismic generated tsunami show a greatly improved fit to both tide gauge and field survey data. Our results highlight a case of a damaging tsunami that's primary source is not seismic. Tsunamis of this nature, while less common, are difficult to provide warning for and are underrepresented in regional tsunami hazard analysis.

1 Introduction

Most tsunamis are generated from slip on faults, often associated with subduction zones. Such is the case for many destructive events of the past century, including the 2004 Sumatra, 2010 Maule, and 2011 Tohoku-Oki earthquakes. These large tsunamis typically exceed run-up heights of 10m (Mori et al., 2011). Occasionally, earthquakes with a strike-slip mechanism will also generate tsunamis, albeit on a smaller, local scale. The 1994 Mindoro Island earthquake in the

Philippines caused measurable (3-4 m) run-ups near the source (Imamura et al.,1995). More recently, the 2010 Haiti earthquake generated a 3m tsunami. Its complex source was a combination of coastal slumping and deformation related to strike-slip motion (Hornbach et al., 2010). The Palu earthquake, with a similar strike-slip mechanism as the Haiti event, ruptured within the Indonesian island of Sulawesi. A portion of the rupture occurred in the narrow Palu Bay, where at its inland terminus, is the city of Palu with a population of over 300,000. It is within this bay where a damaging tsunami occurred. Surveyed run-ups reach 8m with a maximum inundation distance of 430 m (NGDC, 2018). Over 2,200 casualties were reported related to the earthquake, tsunami, and landslides.

The Palu earthquake ruptured in part on the Palu-Koro fault, in a complex tectonic environment (Socquet et al., 2006). The centroid moment tensor (CMT) (USGS, 2018) suggests a left-lateral rupture with a lesser component of normal faulting. This mechanism is consistent with long-term regional strain rate models and tectonic studies (Socquet et al., 2006; Walpersdorf et al., 1998; Bellier et al., 2001; Watkinson and Hall, 2017). While the fault trace of the Palu-Koro fault as well as some secondary local transpressional faults have been mapped, the fault structure through the bay, where the rupture has its tsunamigenic potential, is unknown.

The tsunami is surprisingly large for the associated earthquake magnitude and faulting mechanism. Due to its anomalous behavior, various aspects of the earthquake and tsunami source have garnered recent attention and an extensive scientific discussion has formed over the exact tsunami source mechanism. Direct observations of the tsunami are limited to one near-field tide gauge within the bay and eyewitness accounts. Numerous post-event field surveys have been conducted, providing insight into the inundation, run-up, and damage from the tsunami (Omira et al., 2019; Paulik et al., 2019; Putra et al., 2019). With this data in hand, various studies have provided compelling arguments for pieces of the event. For example, modeling of hypothetical landslides was carried out by Heidarzadeh et al. (2019) and incorporated in Pakoksung et al. (2019), here it was advocated that the dominant landslide that caused the tsunami recorded at the tide gauge was submarine and generated near the entrance of the bay to the northwest. Takagi et al, (2019) focused on one particular subaerial landsliding event near Palu City (southwest of the Pakoksung et al. model) and how it affected inundation in its immediate surroundings, omitting any coseismic effects from the earthquake. Frederik et al., (2019) published post-event bathymetric survey results for non-coastal (> 50 m water depth) parts of Palu Bay, identifying regions that potentially slumped based on the gradient at the expected scarp locations. Sassa et al., (2019) and Arikawa et al., (2019) identified features through field surveys that may have contributed to tsunami waves during the earthquake. Each study provides valuable insight into possible landsliding processes or mechanism. However, no study to date has successfully validated one or multiple landslide sources against field-survey and tide gauge data over the extent of the Palu Bay, nor has landsliding been incorporated into the broader context of the earthquake rupture and its coseismic component.

On the other side of the discussion, additional recent studies have advocated for a tsunami generated through purely co-seismic offsets, without the need to invoke landsliding. Song et al. (2019), for instance, model the event through two rupturing fault segments, deriving a fault model through ascending and descending radar data. Ulrich et al. (2019) also advocates for a coseismic only source model. However, neither study fully recreate and reproduce the run-up and gauge data over the entirety of the bay.

To date, a unifying tsunami model that simultaneously fits the field-survey measurements, the tide gauge amplitude, and the timing of the main tsunami arrival, while also being accurate in modeling the earthquake rupture has not yet been accomplished. The missing link is a model that is self-consistent with the on-shore geodetic data that governs the earthquake rupture as well as and the field-survey and tide gauge data that govern the tsunamigenic behavior over the entire bay. Of the currently published tsunami sources, no model has successfully validated a landslide-driven tsunami with the timing and scale of the tsunami at the local tide gauge nor the regional field survey data. Additionally, no coseismic tsunami model has successfully validated rupture results against regional run-up data.

In this study, we posit that all of these mechanisms, subaerial and submarine landslides, and co-seismic offsets play a role. We systematically explore all possible tsunami sources in addition to the earthquake's rupture near the bay, solving for both coseismic offsets and potential landsliding events in a self-consistent model. First, we focus on the coseismic component of the earthquake, solving for the distributed slip using crustal offset data. Because of ambiguities in the fault geometry, we test three different scenarios. We compute the resultant tsunami for each of the three fault models, ignoring any effects related to landsliding, and compare with tsunami observations. This provides a baseline coseismic tsunami component that is then included in future landsliding models.

Next, we identify potential landsliding events along the coast of Palu Bay. Using satellite imagery, we reconstruct the area lost due to sliding and propose a simple landslide tsunami model. We compare these landsliding events in addition to our best coseismic model to the same observation data as our previous coseismic-only model. The final component of this study is an assessment of potential additional submarine sources. Using a ray-tracing exercise, we outline the locations within Palu Bay that are most likely to contribute to the tsunami, as decided by misfits in run-up and tide gauge data. These locations are modeled and discussed in the context of recently published bathymetric surveys. Our results lead us to conclude that while the co-seismic deformation does contribute to tsunamigenesis, subaerial and submarine landsliding is the more dominant source and is crucial to fitting tide gauge and run-up observations.

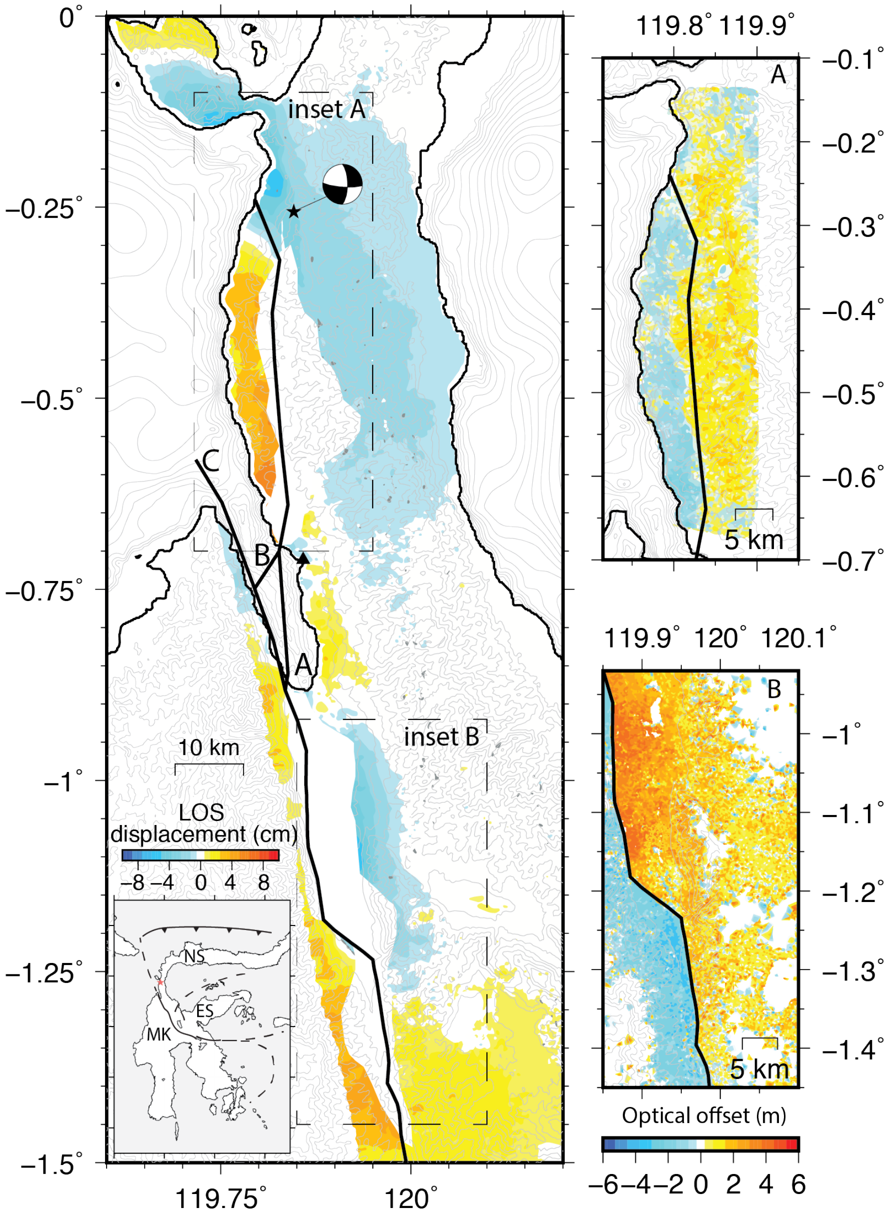

Fig. 1. Static offsets following the Palu earthquake in central Sulawesi. Main figure: unwrapped surface deformation in the line of sight direction. Star indicates the USGS determined epicenter

with corresponding moment tensor. Thick black lines indicate the fault trace for the three potential fault models labeled A, B, and C. Black triangle indicates Pantoloan tide gauge. Inset map: regional view of Sulawesi, including principle faults and presence of three microblocks (MK: Makassar, NS: North Sula, and ES: East Sula) as discussed in Socquet et al., (2006). Insets A and B: optical offsets in the north-south direction. Note a change in color scale between optical and line-of-sight datasets.

2. Data

2.1 Geodetic

We acquired line-of-sight (LOS) crustal deformation using a pair of ascending images from Advanced Land Observation Satellite-2 (ALOS-2) operated by the Japanese Aerospace Exploration Agency (JAXA). The first satellite pass was collected on August 17, 2018 and the second pass was on October 12, 2018. The InSAR data was processed using the GMTSAR (Sandwell et al., 2016) software with outcoming phase unwrapped using SNAPHU (Chen and Zebker, 2013). The post processing was done with GMT (Wessel et al., 2013). The resultant image provides good coverage over the entire Palu Bay region, however some areas immediately adjacent to the inferred fault trace are decorrelated. We sub-sampled the LOS image over the entire model domain, ignoring the offshore and decorrelated masked regions (Fig S1). Our spatial sample rate was every 2 arcminutes in the north-south and east-west directions. This amounts to 631 sample points that were used in the inversion. The maximum deformation in the positive LOS (towards the satellite) direction occurs northwest of Palu Bay with a peak deformation of 4.8 cm (Fig 1). The maximum deformation in the negative LOS (away from satellite) direction is -4.7 cm and occurs in the basin immediately south of Palu City.

In supplement to the InSAR dataset, we incorporate sub-pixel correlation of optical images acquired before and after the earthquake from the Sentinel-2 and Planet labs sensors (Planet Team,

2017) (Table S1). We used an image correlation method (Debella-Gilo and Kääb, 2011) applied to the visible bands, that calculates the normalized cross correlation between the images and achieves sub-pixel precision by interpolating for the correlation peak. To resolve the deformation field to the same scale given the Sentinel-2 and Planet labs imagery have different image resolutions (10 m and 3m, respectively), we used correlation windows with step sizes of 9 and 30 pixels, respectively, resulting in a correlation map of 90 m pixel resolution. Areas of decorrelation are caused primarily by the presence of clouds. However, these occur mostly away from the surface rupture allowing assessment of near-field surface motion. The inclusion of two-dimensional horizontal offset data provides key offset information near the fault trace, where the InSAR dataset is decorrelated.

2.2 Tsunami

The tsunami was recorded at the Pantoloan tide gauge northeast of Palu City (Fig 2). The waveform exhibits two important characteristics that a successful model should recover: the first tsunami arrival time at 5 minutes after origin and an initial reverse polarity signal with a 4 m trough to crest amplitude. The arrival time is a strong constraint on the location of the tsunami source and the large amplitude provides information on the expected scale of seafloor deformation. While it has been postulated that the time recorded on the tide gauge may be inaccurate, the tide gauge observation is consistent with co-located and time-tagged video footage (Carvajal et al., 2019).

Numerous post-event field studies have been published, identifying the extent of damage, tsunami inundation, and run-up (Paulik et al., 2019; Putra et al., 2019; Syamsikik et al., 2019). One such study focusing within the bay (Omira et al., 2019) measured run-up heights at 19 locations in exceedance of 4 m (Fig 2). The coastline immediately northwest of Palu City, near the terminus of Palu Bay, experienced run-ups exceeding 6 m. Near the entrance to and outside of

Palu Bay, there are fewer survey measurements, but run-up heights are lower with one surveyed location measuring 0.9 m. Further to the northeast, no tsunami damage was observed (Omira et al., 2019). We use our tsunami model fits to both the tide gauge timeseries and the run-up data to evaluate each of our earthquake source models.

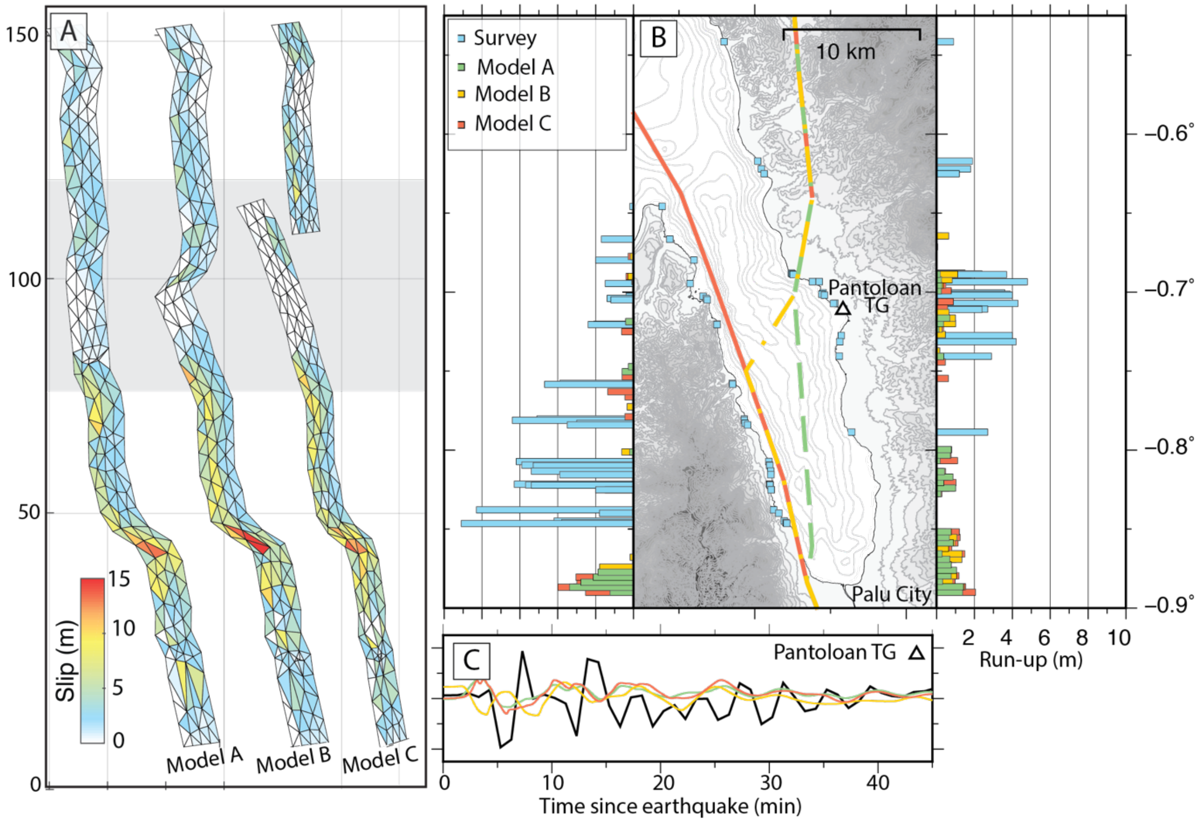

Fig. 2. Finite Fault and tsunami model results for all 3 fault geometries. A: finite fault slip distributions for all three models. Shaded gray region is latitudinal range shown in 2B. B: comparison of observed run-up (blue bars) at coastal locations (blue squares) to modeled run-up (green, yellow, and red bars). Fault traces for each of the three models are included in map view. C: tsunami models against recording at Pantoloan tide gauge (black line).

3. Methods

3.1 Fault Geometry

The geometry of the fault within the bay dictates the location of tsunamigenic seafloor deformation, which in turn can affect tsunami modeling results. The path of the Palu-Koro fault through the bay, as well as how the fault connects to the earthquake's hypocenter to the northeast is unclear. Multiple past geologic studies of the regions as well as more recent modeling work have used a range of fault interpretations (Walpersdorf et al., 1998; Bellier et al., 2006; Socquet et al., 2006; Socquet et al., 2019; Song et al., 2019). Because of the uncertainty, we test three model geometries labeled A, B, and C (Fig 1) all east-dipping at 67° to match the focal mechanism. Based on past GPS surveys, we limit the seismogenic depth to 15 km (Socquet et al., 2006). Each model is discretized using a triangular mesh. We used the three-dimensional finite element mesher GMSH (Geuzaine and Remacle, 2009). The mean size of the bisector of the triangular subfault patches is 3 km. The use of triangles, rather than rectangular patches allows for more complex and bending geometries without subfaults overlapping.

Model A is the simplest and is similar geometry to what has been used in previous studies (Heidarzadeh et al., 2019; Socquet et al., 2019; Song et al., 2019); the northern and southern traces are connected diagonally through the bay. Model B introduces more complexity and connects both sections through a right-stepping restraining bend perpendicular to the bay. Model C meanwhile, has two discontinuous faults, the northern initiating fault, and the Palu-Koro fault extending along the western coast of the bay (Walpersdorf et al., 1998; Bellier et al., 2001; 2006).

3.2 Coseismic Source Inversion

We invert for slip using a non-negative least squares inversion algorithm (Melgar and Bock, 2015) and incorporating equally weighted LOS InSAR and optical offsets from satellite imagery. We used a velocity model that is local to central Sulawesi through CRUST1 (Laske et al., 2013). We employ a Tikhonov regularization scheme and restrict the total moment of our solution to match the USGS determined Mw 7.5 magnitude.

3.3 Landslide Identification

Each subaerial landslide feature was inspect using rapidly acquired satellite imagery through the ESRI Earthquake Disaster Response program (ESRI, 2018). We identified the 11 largest landslides and measured the surface area lost and an estimated scarp length (Figs S2-13). Additional possible landslide events located outside of Palu bay at locations (119.776°E, 0.5317°S), (119.805°E, 0.1499°S), and (119.8181°E, 0.1163°S) are ignored in this study due to a latency between satellite images of over 2 years. We test the tsunamigenic potential of all eleven landslides by modeling each as instantaneous block movements into the bay. This creates a characteristic positive wave in the direction of material deposition (bayward) and a negative wave at the location of excavation (coastal to the collapse). The width of each tsunami source is equal to the width of the scarp. We scale the maximum amplitude of each perturbation to best fit the nearby survey measurements. The satellite timing, landslide scaling, and tsunami model parameters are comprised in Table 1.

ID #	**Longitude**	**Latitude**	**Area (m^2)**	**Scarp Length (m)**	**Amplitude (m)**	**Before Satellite**	**After Satellite**
L01	119.7461	-0.6668	10,972	266	5	9/7/18	10/1/18
L02	119.7871	-0.755	13,278	260	6	9/26/18	9/30/18
L03	119.8055	-0.8012	53,824	711	4	9/26/18	9/30/18
L04	119.8107	-0.8077	10,588	223	4	9/26/18	10/1/18
L05	119.8228	-0.846	35,826	732	5	8/16/18	10/1/18
L06	119.8706	-0.8795	15,324	314	4	8/16/18	10/1/18
L07	119.8627	-0.7896	33,028	530	2	9/26/18	10/1/18
L08	119.8528	-0.7367	20,788	344	3	9/26/18	10/1/18
L09	119.845	-0.7021	39,473	374	3	9/26/18	10/1/18
L10	119.8224	-0.6884	36,507	442	6	9/26/18	10/1/18

L11	119.8113	-0.6302	14,993	411	5	10/24/16	10/1/18

Table 1. Sub-aerial landslide coastal locations and expected area based on land changes between two satellite passes. Amplitude is the seafloor displacement from the landslide and is a tunable parameter.

3.4 Tsunami Modeling

We model all tsunami results using the open source code GeoClaw (LeVeque et al., 2011), which solves the depth-averaged non-linear shallow water wave equations in two-dimensions. We run each model for one hour of propagation time, letting the time step fluctuate to satisfy a preset Courant-Friedrichs-Lewy (CFL) condition of 0.75. The model has a moving boundary condition that allows nodes along the coastline to be wetted and dried throughout the propagation. Bottom friction is achieved using a Manning coefficient of 0.025. We model the tsunami within the bay using 6 s bathymetry and 0.27 s coastal topography from Badan Informasi Geospasial (BIG). We interpolated the bathymetry to the resolution of the coastal data, and in order to lower the computational cost, we use adaptive mesh refinement. Our coarsest mesh is 15 s and the finest mesh, reserved for modeling points of interest along the coast is 1 s with 2 levels of refinement in between.

Run-up is calculated by querying points at the 1 arcsecond spatial scale up to the 15 m elevation contour using the BIG 0.27 s topography DEM. Resulting models were separated into east and west coast points with 0.28 min sized bins along latitude slices. The elevation at the furthest measurable extent of the tsunami in each bin is recorded as the model run-up. Due to multiple observed run-ups within the same latitude, the survey dataset (Omira et al., 2019) is plotted as is for comparison and is not binned.

We assess the goodness of fit of the tsunami model to the tide gauge measurement using the normalized root mean square misfit (NRMS) method (Heidarzadeh et al., 2016). We interpolate the tide gauge and modeled waveform to the same sample rate and concentrate on the first 10 minutes of observed and modeled tsunami waveforms to capture both the trough and then crest of the initial wave as well as its delayed arrival. A perfect fit corresponds to a NRMS of 0. All NRMS fits are included in Table 2.

Table 2: Normalized RMS misfit values for each tsunami model. Misfit is calculated for the first 10 minutes of tsunami propagation.

Model	NRMS
Model A	1.0110
Model B	1.3457
Model C	1.0004
Model C + Landslides	0.9509
Model C + Landslides + Submarine	0.7379

4. Results

4.1 A Coseismic Source?

Our three finite fault models (Fig 2a) reveal a consistent behavior despite slight differences in fault geometry through Palu Bay. Slip northeast of the bay, where the earthquake initiated is dominantly strike-slip and shallow (< 5 km). As the fault enters the bay, slip diminishes before resuming south of Palu City. Slip in this southern section extends down to 15 km with a narrow yet continuous band of slip in exceedance of 5 m at a depth of about 10 km. Along the releasing bend south of Palu City, normal faulting is also observed. Our coseismic model fits the north-south offsets of the optical dataset well but does underestimate LOS deformation further from the fault trace (Figs S14-16). While slip does occur within the bay in some of our models, it is constrained to strike-slip motion, and does not produce large vertical offsets.

Due to the diminished slip within the bay and its strike-slip nature, the tsunamigenic potential of all coseismic finite-fault models is low. When compared to the observed run-up in Fig 2b, the seismically generated tsunami largely underestimates the observations throughout the bay. The only area where moderate (~ 2 m) run-up is modeled is along the southern coastline. At the Pantoloan tide gauge (Fig. 2c) the model fails to recreate both the large trough to crest amplitude and the arrival time.

Indubitably a coseismic component to the tsunami must exist and yet all three models have similar seafloor deformation (Fig S17). For further exploration of additional sources, we continue using model C as a baseline for the coseismic tsunamigenic behavior. We favor this model because it includes the Palu-Koro fault as it extends through the bay, which previous studies (Walpersdorf et al.,1998; Bellier et al., 2001) have confirmed the trace of. The possibility of the fault running north-south through the bay, rather than bending, is also corroborated by recent bathymetric surveying (Frederick et al., 2019). Meanwhile models A and B assume a connection to secondary faults that have not been tectonically validated. The tsunami waveform from Model C also has the lowest normalized root mean square misfit (Table 2).

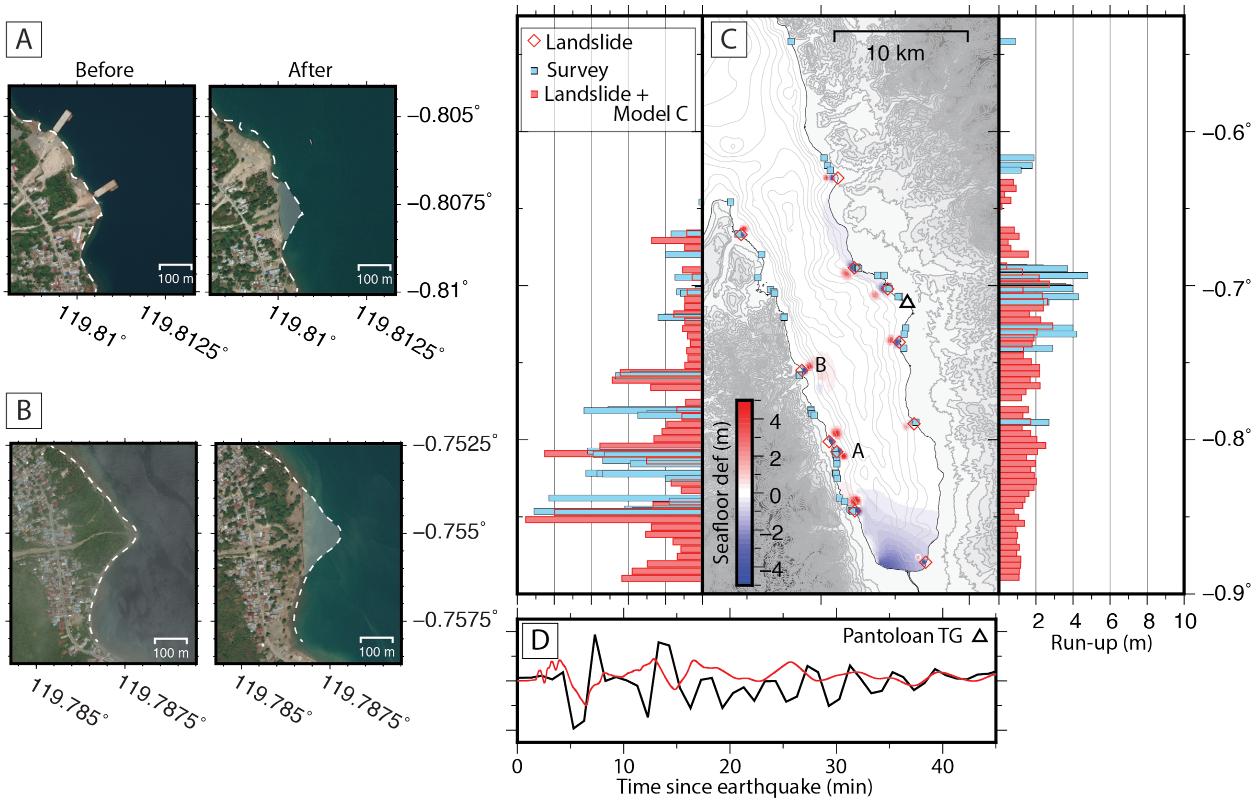

Fig 3. A and B. Before and after imagery showing coastal collapse on the west side of Palu Bay. Further information on satellite imagery and surface area loss in Table 1. **C**. Comparison of observed run-up (blue bars) to modeled run-ups (red bars) for a combined landslide and model C source. Shaded deformation within the map view shows the initial vertical seafloor offsets from landslide and model C. Seafloor deformation for the other two finite fault models is shown in Fig S5. Tide gauge indicated by a white triangle. **D.** Comparison of observed waveform (black) to model (red) for the first 45 minutes following the start of the earthquake.

4.2 A Landslide Source?

With the addition of contemporaneous landslide sources, the fit to the observed run-up is greatly improved (Fig 3). Through the use of small near-point sources, we are able to match the high spatial variability in run-ups along the eastern and western coastlines. For example, on the western coast of Palu bay 8+ m run-ups are recreated without creating equally large yet unobserved run-ups on the eastern coast. However, while the survey data is largely recreated, an inconsistency remains: the inclusion of sub-aerial sources does not sufficiently improve the waveform fit at the

Pantoloan tide gauge. Sources on the scale of the landslides that we observe do not produce waves that effectively propagate across the bay, nor with the 6-minute period observed at the tide gauge.

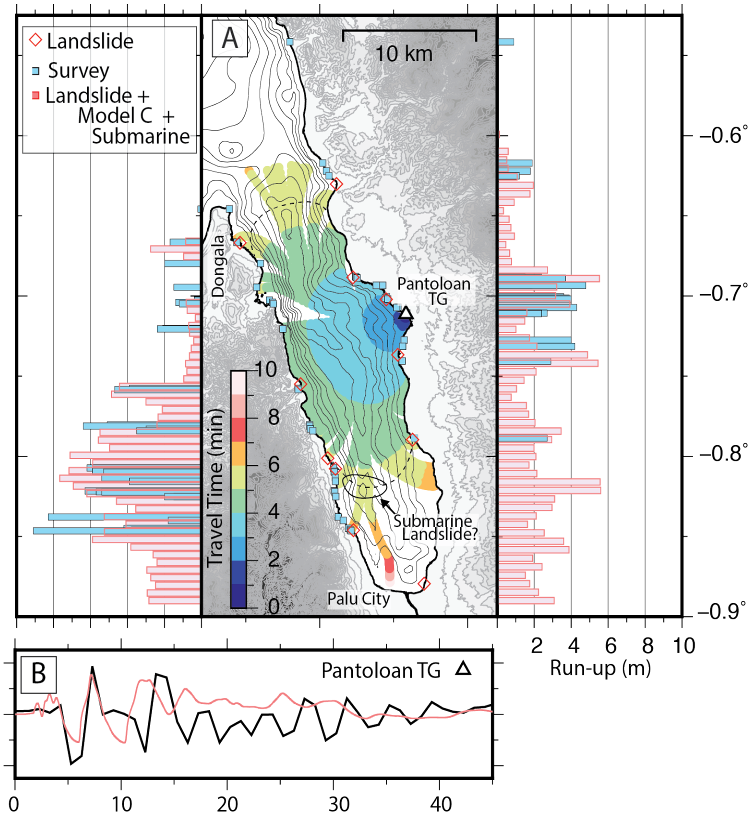

Figure 4. **A**. Tsunami ray tracing results within Palu Bay and tsunami model outputs for a coseismic, subaerial, submarine combined model. Black dashed line shows the needed nucleation point for a tsunami corresponding with the largest trough at Pantoloan tide gauge (white triangle). The additional needed submarine location is outline; seafloor deformation is shown in figure S5. Bathymetric contours have a 100 m spacing. **B**. Comparison between observed (black line) and modeled (pink line) tsunamis at tide gauge for the first 30 minutes following the earthquake.

In order to explain this last piece of the tsunami observations, we hypothesize an additional submarine landslide component whose locations and extent can be constrained from a ray-tracing analysis (Gusman et al., 2017) of the travel time from the gauge into the bay (Fig 4a). By assuming a reciprocity principle between source and receiver (Hossen et al., 2015) we identify regions where an additional tsunami component could nucleate and reach the tide gauge at the arrival of the first large negative wave. We find that a source originating within the port of Pantoloan would arrive at the tide gauge in under 2 minutes, a source from directly across the bay would arrive within 4 minutes, and a source located near Palu City would take up to 10 minutes to reach the gauge.

The areas where a tsunami source would best explain the tide gauge's arrival time are to the north of Pantoloan, near Dongala, and south, between Pantoloan and Palu City (Fig 4a). By incorporating one additional offshore tsunami source, we are able to recover the arrival time and most of the amplitude at the tide gauge, as well as the field survey run-up (Fig 4). We scale the size and amplitude of the source to match the wavelength and peak amplitude of the tide gauge signal. While the coastal run-up is best described by small, high amplitude sources, the tide gauge fits best with a wider, yet low amplitude source (Fig S17).

We prefer the inclusion of the southern submarine landslide source because it occurs in an area that has steep bathymetry, is near two coastal landslide sites, and coincides with the highest observed run-ups within Palu Bay. Additionally, our inferred southern submarine source is near to the location of a possibly identified seafloor slump (Takagi et al., 2019). Possible source locations north of Pantoloan, while arriving at the tide gauge at the correct time and as advocated for in Pakoksung et al., (2019), would contradict the comparatively low (2 m to the north vs 6 m to the south) observed run-up values. A source to the southeast, while also plausible, would occur in an area with a much gentler bathymetric slope.

5. Discussion

With all three tsunamigenic components: the modest coseismic deformation, the subaerial landslides, and the inclusion of a deeper submarine slump, the signal at the tide gauge, and the survey run-ups are largely recovered. One small difference, however, is that the final synthetic tide gauge model has higher frequency waves, due to coastal landslide sources arriving prior to the main tsunamigenic component at 5 minutes. These cannot be seen in the real record, possibly due to the low 60s sampling rate. Though without the inclusion of these landslide sources, the run-up in the near-field is largely underestimated. These timing of these early high frequency waves are corroborated with video footage from the inside the bay and close to the tide gauge (Carvajal et al., 2019).

The inclusion of the additional submarine landsliding component is the last piece to the puzzle explaining the size of the tsunami. However, while the coastal landslides are visible through rapidly acquired satellite imagery following the event, it is much harder to determine the veracity of submarine sources. We postulate that the large number of mass failures do not simply stop at the water line but rather would continue along steeper submarine slopes within the bay. While detailed seafloor surveies following the Palu event exist (Fredrik et al., 2019), the resolution is limited to locations within the bay at depths of greater than 50 m, which largely excludes the coast near the subaerial landslides.

In complement to seafloor surveys, ray tracing helps to narrow down possible tsunami source locations that would arrive at the local tide gauge with the appropriate timing. This requires high resolution bathymetry and coastal DEMs as the tsunami's velocity is dependent on the water depth. Since Palu bay is so narrow, only 5 km across, changes in water depth between coarser and finer models can greatly affect the ray tracing solution. In this study we use the finest scale bathymetry and coastal DEMs available through BIG. The higher resolution bathymetry recovers features within the bay that are not seen in coarser models, which affects tsunami propagation for both modeling purposes as well as ray tracing.

The results of ray tracing allow us to exclude scenarios where coseismic slip on submarine faults generate a tsunami with too early of an arrival time. Many postulated fault geometries with moderate coseismic slip, particularly through the use of a restraining bend or other exotic geometries (Heidarzadeh et al., 2019; Song et al., 2019; Ulrich et al., 2019) to promote tsunamigenic vertical deformation on the seafloor occur within the area described by the ray tracing exercise as too close to the tide gauge to have the correct tsunami arrival time. While it could be argued that the timing on the tide gauge is perhaps erroneous or inaccurate (Heidarzadeh et al., 2019), video footage local to Pantoloan confirms the main tsunami arrival time (Carvajal et al., 2019). Ray tracing also allows us to narrow down the submarine component to a few candidate locations. Analysis of recent field-surveys allows us to further narrow down the locations of possible tsunami sources. Our prioritization of southern Palu Bay tsunami sources fits well with the extreme local run-up. Large tsunami sources, either coseismically or through landsliding, located at the entrance to, or outside of Palu Bay simply contradict the results of field surveys that show little damage and low run-ups at those localities (Omira et al., 2019).

The Palu tsunami represents a complex tsunamigenic scenario where the earthquake was a contributor, but not the primary cause of the tsunami. Instead the earthquake likely triggered the landsliding that produced the damaging waves. Bao et al. (2019) and Socquet et al. (2019) both conclude in separate studies that the earthquake was likely a super-shear rupture. These events can generate stronger than normal shaking which could act as the impetus for the large number and wide spatial distribution of mass wasting throughout the bay. Super-shear ruptures are thought to be more prevalent along strike-slip faults. While these are traditionally less tsunamigenic environments, the Palu tsunami proves that exceptions to this assumption do occur. Understanding these exceptional events is important not just for the region of Sulawesi but for other places where there are offshore strike-slip faults such as California, Greece, Turkey, Western Canada and Alaska. As postulated (Mai, 2019), other strike-slip faults like the San Andreas and North Anatolian faults intersect bodies of water and may be susceptible to similar tsunami hazards as

Palu Bay. Similar events as this are also a potential threat in environments where non-seismic landslides are already common and are paired with an expected future seismic hazard such as parts of the U.S. Pacific Northwest.

6 Conclusion

We conclude that while the co-seismic source contributes, the Palu tsunami is devastating primarily because of subaerial and submarine landsliding. The likelihood landslide tsunamis may be enhanced by the elevated shaking associated with supershear ruptures as was likely the case here (Socquet et al., 2019; Bao et al., 2019). Landslide induced tsunamis, particularly in narrow bays near large population centers pose a difficult challenge for tsunami hazard assessment. Our model, as well as field observations, show a devastating tsunami that inundated nearly all coasts in the bay within 5 minutes. Even with state-of-the-art warning systems, it would be highly challenging to give sufficient lead-time to prevent a catastrophe as occurred during the Palu event. Nonetheless, the identification and inclusion of future landslide induced tsunami sources should continue to be a priority in regional tsunami hazard assessments.

Acknowledgments

This project was funded in part through NASA ROSES grant number 80NSSC19K0360. Figures were made using Generic Mapping Tools (Wessel et al., 2013). Advanced Land Observing Satellite-2 (ALOS-2) data were provided by the Japan Aerospace Exploration Agency under investigation 1148. The MudPy source inversion code can be found at https://github.com/dmelgarm/mudpy/. The GeoCalw tsunami modeling code can be obtained from https://www.clawpack.org/. The tsunami record, unwrapped InSAR scenes, and visible imagery are available from the corresponding author upon request. We thank Aditya Gusman for access to the tsunami ray tracing code, it can be found at https://github.com/adityagusman/tsunami-raytracing. We also thank Joern Behrens and Elizabeth Madden for helpful discussions.

References

Arikawa, T., Muhari, A., Okumura, Y., Dohi, Y., Afriyanto, B., Sujatmiko, K. A., & Imamura, F. (2018). Coastal subsidence induced several tsunamis during the 2018 Sulawesi earthquake. *Journal of Disaster Research*, *13*, 1-3.

Bao, H., Ampuero, J. P., Meng, L., Fielding, E. J., Liang, C., Milliner, C. W. D., … Huang, H. (2019). Early and persistent supershear rupture of the 2018 magnitude 7.5 Palu earthquake. *Nature Geoscience*. https://doi.org/10.1038/s41561-018-0297-z

Bellier, O., Siame, L., Beaudouin, T., Villeneuve, M., & Braucher, R. (2001). High slip rate for a low seismicity along the Palu-Koro active fault in Central Sulawesi (Indonesia). *Terra Nova*, *13*(6), 463–470. https://doi.org/10.1046/j.1365-3121.2001.00382.x

Bellier, O., Sébrier, M., Seward, D., Beaudouin, T., Villeneuve, M., & Putranto, E. (2006). Fission track and fault kinematics analyses for new insight into the Late Cenozoic tectonic regime changes in West-Central Sulawesi (Indonesia). *Tectonophysics*, *413*(3-4), 201-220.

Carvajal, M., Araya-Cornejo, C., Sepúlveda, I., Melnick, D., & Haase, J. S. (2019). Nearly-instantaneous tsunamis following the Mw 7.5 2018 Palu earthquake. *Geophysical Research Letters*, 2019GL082578. https://doi.org/10.1029/2019GL082578

Chen, A. C., & Zebker, H. A. (2013). Reducing ionospheric effects in InSAR data using accurate coregistration. *IEEE transactions on geoscience and remote sensing*, *52*(1), 60-70.

Debella-Gilo, M., & Kääb, A. (2011). Sub-pixel precision image matching for measuring surface displacements on mass movements using normalized cross-correlation. *Remote Sensing of Environment*, *115*(1), 130-142.

ESRI. (2018). Disaster Response Program. https://www.esri.com/en-us/disaster-response/disasters/earthquakes

Frederik, M. C., Adhitama, R., Hananto, N. D., Sahabuddin, S., Irfan, M., Moefti, O., ... & Riyalda, B. F. (2019). First results of a bathymetric survey of Palu Bay, Central Sulawesi, Indonesia following the Tsunamigenic Earthquake of 28 September 2018. *Pure and Applied Geophysics*, *176*(8), 3277-3290.

Geuzaine, C., & Remacle, J. F. (2009). Gmsh: A 3-D finite element mesh generator with built-in pre-and post-processing facilities. *International journal for numerical methods in engineering*, *79*(11), 1309-1331.

Gusman, A. R., Satake, K., Shinohara, M., Sakai, S. I., & Tanioka, Y. (2017). Fault slip distribution of the 2016 Fukushima earthquake estimated from tsunami waveforms. *Pure and Applied Geophysics*, *174*(8), 2925-2943.

Heidarzadeh, M., Murotani, S., Satake, K., Ishibe, T., & Gusman, A. R. (2016). Source model of the 16 September 2015 Illapel, Chile, Mw 8.4 earthquake based on teleseismic and tsunami data. *Geophysical Research Letters*, *43*(2), 643-650.

Heidarzadeh, M., Muhari, A., & Wijanarto, A. B. (2019). Insights on the Source of the 28 September 2018 Sulawesi Tsunami, Indonesia Based on Spectral Analyses and Numerical Simulations. *Pure and Applied Geophysics*, *176*(1), 25–43. https://doi.org/10.1007/s00024-018-2065-9

Hornbach, M. J., Braudy, N., Briggs, R. W., Cormier, M. H., Davis, M. B., Diebold, J. B., … Templeton, J. (2010). High tsunami frequency as a result of combined strike-slip faulting and coastal landslides. *Nature Geoscience*, *3*(11), 783–788. https://doi.org/10.1038/ngeo975

Hossen, M. J., Cummins, P. R., Roberts, S. G., & Allgeyer, S. (2015). Time reversal imaging of the tsunami source. *Pure and Applied Geophysics*, *172*(3-4), 969-984.

Imamura, F., Synolakis, C. E., Gica, E., Titov, V., Listanco, E., & Lee, H. J. (1995). Field survey of the 1994 Mindoro Island, Philippines tsunami. *pure and applied geophysics*, *144*(3-4), 875-890.

Laske, G., Masters, G., Ma, Z., & Pasyanos, M. (2013, April). Update on CRUST1. 0—A 1-degree global model of Earth's crust. In *Geophys. Res. Abstr* (Vol. 15, p. 2658). Vienna, Austria: EGU General Assembly.

LeVeque, R. J., George, D. L., & Berger, M. J. (2011). Tsunami modelling with adaptively refined finite volume methods. *Acta Numerica*, *20*, 211-289.

Mai, P. M. (2019). Supershear tsunami disaster. *Nature Geoscience*. https://doi.org/10.1038/s41561-019-0308-8

Melgar, D., & Bock, Y. (2015). Kinematic earthquake source inversion and tsunami runup prediction with regional geophysical data. *Journal of Geophysical Research: Solid Earth*, *120*(5), 3324-3349.

Mori, N., Takahashi, T., Yasuda, T., & Yanagisawa, H. (2011). Survey of 2011 Tohoku earthquake tsunami inundation and run-up. *Geophysical Research Letters*, *38*(18), 6–11. https://doi.org/10.1029/2011GL049210

National Geophysical Data Center, NGDC, 2018

Omira, R., Dogan, G. G., Hidayat, R., Husrin, S., Prasetya, G., Annunziato, A., … Yalciner, A. C. (2019). The September 28th, 2018, Tsunami In Palu-Sulawesi, Indonesia: A Post-Event Field Survey. *Pure and Applied Geophysics*, *176*(4), 1379–1395. https://doi.org/10.1007/s00024-019-02145-z

Pakoksung, K., Suppasri, A., Imamura, F., Athanasius, C., Omang, A., & Muhari, A. (2019). Simulation of the Submarine Landslide Tsunami on 28 September 2018 in Palu Bay, Sulawesi Island, Indonesia, Using a Two-Layer Model. *Pure and Applied Geophysics*, 1-28.

Paulik, R., Gusman, A., Williams, J. H., Pratama, G. M., Lin, S. L., Prawirabhakti, A., ... & Suwarni, N. W. I. (2019). Tsunami hazard and built environment damage observations from Palu City after the September 28 2018 Sulawesi earthquake and tsunami. *Pure and Applied Geophysics*, *176*(8), 3305-3321.

Planet Team, 2018

Putra, P. S., Aswan, A., Maryunani, K. A., Yulianto, E., & Kongko, W. (2019). Field survey of the 2018 Sulawesi tsunami deposits. *Pure and Applied Geophysics*, 1-11.

Sandwell, D., Mellors, R., Tong, X., Wei, M., & Wessel, P. (2011). Gmtsar: An insar processing system based on generic mapping tools.

Sassa, S., & Takagawa, T. (2019). Liquefied gravity flow-induced tsunami: first evidence and comparison from the 2018 Indonesia Sulawesi earthquake and tsunami disasters. *Landslides*, *16*(1), 195-200.

Socquet, A., Hollingsworth, J., Pathier, E., & Bouchon, M. (2019). Evidence of supershear during the 2018 magnitude 7.5 Palu earthquake from space geodesy. *Nature Geoscience*. https://doi.org/10.1038/s41561-018-0296-0

Socquet, A., Simons, W., Vigny, C., McCaffrey, R., Subarya, C., Sarsito, D., … Spakman, W. (2006). Microblock rotations and fault coupling in SE Asia triple junction (Sulawesi, Indonesia) from GPS and earthquake slip vector data. *Journal of Geophysical Research: Solid Earth*, *111*(8). https://doi.org/10.1029/2005JB003963

Song, X., Zhang, Y., Shan, X., Liu, Y., Gong, W., & Qu, C. (2019). Geodetic Observations of the 2018 Mw 7.5 Sulawesi Earthquake and Its Implications for the Kinematics of the Palu Fault. *Geophysical Research Letters*. https://doi.org/10.1029/2019GL082045

Ulrich, T., Vater, S., Madden, E. H., Behrens, J., van Dinther, Y., van Zelst, I., ... & Gabriel, A. A. (2019). Coupled, Physics-based Modeling Reveals Earthquake Displacements are Critical to the 2018 Palu, Sulawesi Tsunami. *Pure and Applied Geophysics*, 1-41.

United States Geologic Survey, USGS (2018).

Walpersdorf, A., Vigny, C., Subarya, C., & Manurung, P. (1998). Monitoring of the Palu-Koro Fault (Sulawesi) by GPS. *Geophysical Research Letters*, *25*(13), 2313–2316. https://doi.org/10.1029/98GL01799

Watkinson, I. M., & Hall, R. (2017). Fault systems of the eastern Indonesian triple junction: evaluation of Quaternary activity and implications for seismic hazards. *Geological Society, London, Special Publications*, *441*(1), 71–120. https://doi.org/10.1144/SP441.8

Wessel, P., Smith, W. H., Scharroo, R., Luis, J., & Wobbe, F. (2013). Generic mapping tools: improved version released. *Eos, Transactions American Geophysical Union*, *94*(45), 409-410.